Research Article

Facile construction of highly efficient MOF-based Pd@UiO-66-NH$_2$@ZnIn$_2$S$_4$ flower-like nanocomposites for visible-light-driven photocatalytic hydrogen production

Mengting Cao, Fengli Yang, Quan Zhang, Juhua Zhang, Lu Zhang, Lingfeng Li, Xiaohao Wang, Wei-Lin Dai*

Department of Chemistry and Shanghai Key Laboratory of Molecular Catalysis and Innovative Materials, Fudan University, Shanghai 200438, China

ARTICLE INFO

ABSTRACT

Construction of metal-organic-frameworks-based composite photocatalysts has attracted much attention for the reasonable band gap and high surface areas to improve the photocatalytic activity. In this study, the ternary heterojunction Pd@UiO-66-NH$_2$@ZnIn$_2$S$_4$ nanocomposites were facilely prepared for the first time by a two-step method. The visible-light-promoted hydrogen production rate of 0.3 % Pd@UiO-66-NH$_2$@ ZnIn$_2$S$_4$ reaches up to 5.26 mmol g^{-1} h^{-1}, which is evidently much higher than pure UiO-66-NH$_2$, ZnIn$_2$S$_4$ and binary UiO-66-NH$_2$/ZnIn$_2$S$_4$ composites. Such a huge improvement in the photocatalytic performance is mainly attributed to the matched band gap of ZnIn$_2$S$_4$ and UiO-66-NH$_2$, and the introduction of Pd NPs into photocatalysts that broaden spectral response range and promote the photon induced charge carrier separation. This work may provide a feasible approach for the design and construction of metal-organic-frameworks-based photocatalytic materials.

© 2021 Published by Elsevier Ltd on behalf of The editorial office of Journal of Materials Science & Technology.

1. Introduction

With the development of economy and technology, energy demand has been increasing in the modern world. People are devoted to searching for sustainable energy to deal with current energy and environmental crisis. Hydrogen energy is an important branch of new energy, whose representative reaction is light-driven water splitting for hydrogen production [1]. Accordingly, great progress has been made in the research of efficient photocatalysts for hydrogen production [2,3], such as g-C$_3$N$_4$ [4], Cu$_2$O [5], BiVO$_4$ [6], CdS [7], and other semiconductor materials [8–13]. However, the wide band gap and rapid recombination rate of photogenerated electron-hole pairs of photocatalytic materials result in low visible-light photocatalytic activity, which limits the practical applications. Thus, it is necessary to construct efficient photocatalysts that can be used in new energy and environmental protection.

Transition metal chalcogenides have narrower band gaps than their corresponding metal oxide with a good response in the visible light region [14–16]. ZnIn$_2$S$_4$, as one of the representatives of ternary metal chalcogenides, is known to all for the lowcost, stability, and excellent catalytic performance [17]. Nevertheless, the narrow band gap and the rapid recombination of photo-generated electron-hole pairs result in a poor photocatalytic hydrogen production activity of pure ZnIn$_2$S$_4$ [18]. Notwithstanding, due to the cost efficiency in practical application, it is necessary to take strategies to modify ZnIn$_2$S$_4$ for improving the photocatalytic activity.

Recently, metal-organic frameworks (MOFs) as an emerging material possessing high surface areas and tunable porous structures have attracted much attention among scientists [19]. Many MOFs have been reported to behave as semiconductors that have been applied to photocatalysis systems, such as organic pollutants degradation [20] and conversion of solar energy [21]. Besides, the diversity of MOF structure provides better function than inorganic semiconductors [22]. Therefore, researchers work on constructing different MOF/inorganic semiconductors with a reasonable band gap by adjusting the organic linker, encapsulating noble-metal nanoparticles into MOF pores, or compositing real semiconductors. With the continuous research, many catalysts such as ZnO@ZIF-8 [23], Cu$_3$(BTC)$_2$@TiO$_2$ [24], BiVO$_4$@MIL-101 [25], Bi$_2$WO$_6$@UiO-66 [26], BiOBr@UiO-66 [27], UiO-66@g-C$_3$N$_4$ [28], CdS@UiO-66-NH$_2$ [29], MoS$_2$@UiO-66@CdS [30] and Cd$_{0.2}$Zn$_{0.8}$S@UiO-66-NH$_2$ [31] have been designed to promote the photocatalytic activity.

* Corresponding author.
E-mail address: wldai@fudan.edu.cn (W.-L. Dai).
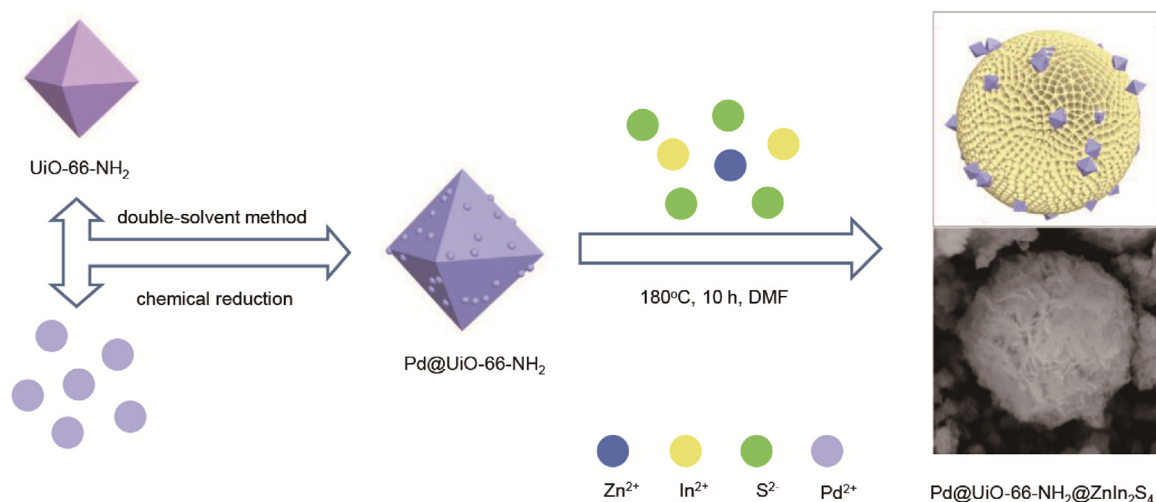
Scheme 1. Schematic illustration of the synthetic process for Pd@UiO-66-NH$_2$@ZnIn$_2$S$_4$ composites.

Metal nanoparticles (such as Pt, Pd, Ag) loaded on semiconductors have exhibited an excellent perspective for improving the photocatalytic activity of MOFs [32,33]. On the one hand, metal nanoparticles with lower Fermi energy level of the metal conduction potential can broaden the spectral response range and promote the photon-induced charge carrier separation [34,35]. On the other hand, the conduction electrons of the semiconductor can be injected into noble metals for effective participation in the catalysis. What's more, the uniform and ordered pores in MOFs provide well-defined microenvironments that can control the size of metal nanoparticles, and the organic ligands can act as anchors to stabilize these nanoparticles [36,37].

Herein, in this work, for the first time, we combined Pd-loaded UiO-66-NH$_2$ with ZnIn$_2$S$_4$ as two candidates for the construction of a new ternary heterojunction Pd@UiO-66-NH$_2$@ZnIn$_2$S$_4$ composites through a facile two-step method. And the morphology, structure, and optical characteristics were investigated by SEM (scanning electron microscopy), TEM (transmission electron microscopy), XPS (X-ray photoelectron spectroscopy), XRD (X-ray diffraction), UV–vis. DRS (ultraviolet-visible diffuse reflectance spectra) and so on. Compared with pure UiO-66-NH$_2$, ZnIn$_2$S$_4$ and UiO-66-NH$_2$/ZnIn$_2$S$_4$, the as-prepared Pd@UiO-66-NH$_2$@ZnIn$_2$S$_4$ showed much better performance for the light-driven hydrogen production reaction, and 0.3 % Pd@UiO-66-NH$_2$@ZnIn$_2$S$_4$ had the best performance in these materials, reaching up to 5.26 mmol g^{-1} h^{-1} under visible light irradiation. The relationship of physicochemical property and the photocatalytic activity were also correlated to explore the possible catalytic mechanism.

2. Experimental

All chemicals were analytical reagent grade obtained from commercial sources and used directly without further purification.

2.1. Synthesis of UiO-66-NH$_2$

The synthesis was carried out via a typical method [38] with some improvements. ZrCl$_4$ (1 mmol, 0.2332 g), 2-aminoterephthalic acid (1 mmol, 0.1812 g), and benzoic acid (20.45 mmol, 2.5 g) were added to a beaker containing 60 mL of DMF. After stirring for 1 h, the above mixture was transferred to a volume of 100 mL Teflon-lined autoclave and maintained at 120 °C for 24 h. After cooling to room temperature, the solid was washed with DMF and methanol several times by centrifugation, dried at 80 °C. The sample was labeled as UN.

2.2. Synthesis of Pd@UiO-66-NH$_2$

Pd@UiO-66-NH$_2$ was prepared according to the previously reported double-solvent method with a chemical reduction [39]. UiO-66-NH$_2$ was activated at 150 °C under vacuum for 12 h to remove the residual solvent in the pores. Then, 100 mg of activated UiO-66-NH$_2$ was sonicated in 20 mL of anhydrous n-hexane for 30 min. Subsequently, PdCl$_2$ aqueous (0.94 M) was added in several minutes under constant stirring and the suspension was continuously stirred for 3 h. After that, the newly prepared NaBH$_4$ solution was added drop by drop and stirred for another 1 h. The solid was washed with ethanol several times by centrifugation, dried at 80 °C. When 10, 20, 30, 40, 50 μL of PdCl$_2$ aqueous were added, the corresponding composites were labeled as PU-x (PU-1, PU-2, PU-3, PU-4 and PU-5). Pd/ZnIn$_2$S$_4$ was prepared by the same method, labeled as Pd/ZIS.

2.3. Synthesis of Pd@UiO-66-NH$_2$@ZnIn$_2$S$_4$

The complete synthetic route is schematically illustrated in Scheme 1. 47 mg of Pd@UiO-66-NH$_2$ powder (PU-x) was dispersed in 30 mL of DMF and sonicated for 30 min, followed by the addition of ZnCl$_2$ (1 mmol, 0.136 g), InCl$_3$·4H$_2$O (2 mmol, 0.586 g), and TAA (4 mmol, 0. 301 g). The mixture was stirred for 30 min and then transferred to a volume of 100 mL Teflon-lined autoclave, maintained at 180 °C for 10 h. After cooling to room temperature, the solid was washed with DMF and methanol several times by centrifugation, dried at 80 °C overnight. The samples were labeled as PUZ-x (PUZ-1, PUZ-2, PUZ-3, PUZ-4, and PUZ-5). Pure ZnIn$_2$S$_4$ and UiO-66-NH$_2$/ZnIn$_2$S$_4$ were prepared by the same method, labeled as ZIS and UZ.

2.4. Synthesis of Pt@UiO-66-NH$_2$@ZnIn$_2$S$_4$, Ag@UiO-66-NH$_2$@ZnIn$_2$S$_4$, and Cu@UiO-66-NH$_2$@ZnIn$_2$S$_4$

A variety of noble metal NPs loaded on photocatalysts were synthesized by similar experimental methods, including Pt@UiO-66-NH$_2$@ZnIn$_2$S$_4$, Ag@UiO-66-NH$_2$@ZnIn$_2$S$_4$, and Cu@UiO-66-NH$_2$@ZnIn$_2$S$_4$ as a comparison, labeled as PtUZ, AgUZ, and CuUZ.

2.5. Materials characterization

The phase composition and crystalline nature were obtained on a D2 phaser X-ray diffractometer. SEM images were observed on a scanning electron microscope (Phenom Prox). TEM and HRTEM

images were attained using a transmission electron microscope (JOEL JEM 2011) operated at an accelerating voltage of 200 kV. XPS measurements were performed with an RBD 147 upgraded Perkin Elmer PHI 5000C ESCA system using Mg K_α radiation. And contaminant carbon (C 1s = 284.6 eV) was used to calibrate all binding energies. FT-IR experiment was carried out with a Nicolet iS10 Fourier Transform Infra-Red spectrometer. The band gaps of the samples were measured by ultraviolet visible diffuse reflectance spectroscopy (UV–vis. DRS) carried out with a PERKIN ELMER Lambda 650S spectrophotometer with BaSO$_4$ used as a reference. Photoluminescence (PL) spectra of powders were obtained with a VARIAN CARY ECLIPSE fluorescence spectrophotometer at the emission wavelength of 370 nm.

2.6. Photocatalytic activity tests

The photocatalytic hydrogen production reactions were carried out in a gas recirculating closed system using a CEL-HXF300 300 W Xe arc lamp at 20 °C, and a cut-off filter (λ > 420 nm) was used to provide the visible light irradiation. 20 mg of the photocatalyst was dispersed in 100 mL aqueous solution of triethanolamine (TEOA) (10 vol.%), with different proportions of H$_2$PdCl$_4$ or H$_2$PtCl$_6$ aqueous solution added as a control. Then, the system was degassed and irradiated. The gases produced were analyzed through a gas chromatograph fitted out with a 5 Å molecular sieve column and a thermal conductivity detector.

2.7. Photoelectrochemical tests

The electrochemical measurements were carried out by using an electrochemical station and an electrochemical analyzer (CHI 760E) in a standard three-electrode quartz cell. The working electrode of photocurrent was prepared as follows: the sample (2 mg) was ultrasonically dispersed in 1.0 mL of ethanol solution and then the mixture was applied to a clean FTO glass with a working area of 1 cm^2. After dried at 100 °C for 6 h, the FTO glass was used as the working electrode, with a platinum plate as a counter electrode and an Ag/AgCl reference electrode. The transient photocurrent response of the different samples was determined in a 0.2 M Na$_2$SO$_4$ aqueous solution under the irradiation of a 300 W Xe lamp without filter. EIS measurements were determined with the frequency range of 10^5 to 10^{-2} Hz in a 0.2 M Na$_2$SO$_4$ aqueous solution.

3. Results and discussion

3.1. Characterizations

The phase structures of the PU-x and PUZ-x catalysts with different mass ratios were determined by XRD. As shown in Fig. 1, pure UN has the diffraction peaks at 2θ of 7.4°, 8.5°, 25.8°, 28.9°, and 30.8° as reported in Ref. [40]. Compared to pure UN, the crystallinity of PU-x composites is unchanged even though Pd was loaded on UN by the double-solvent method and chemical reduction (Fig. S1 in Supporting Information), which indicates that the as-prepared PU-x composites still maintain the integrity of MOFs. In addition, the slight shift of peak positions and the decrease of peak strength in the composites show a certain interaction between Pd and UN [41]. The main peaks of pure ZIS at 2θ of 7.5°, 21.4°, 27.5°, 28.9°, 47.9°, 52.8°, and 56.0° are assigned to the diffraction planes (002), (006), (102), (104), (110), (116), and (022) of ZIS (JCPDS no.65-2023) [42]. After compounded with PU-x, the peaks belonging to ZIS in PUZ-x shift to a low angle direction, and the diffraction peaks belonging to UN are observed, exhibiting that PU-x and ZIS were successfully composited with a strong interaction between them. There is no diffraction peak of Pd in the patterns, which may be due to its low content or the interference of other peaks. The existence of Pd in
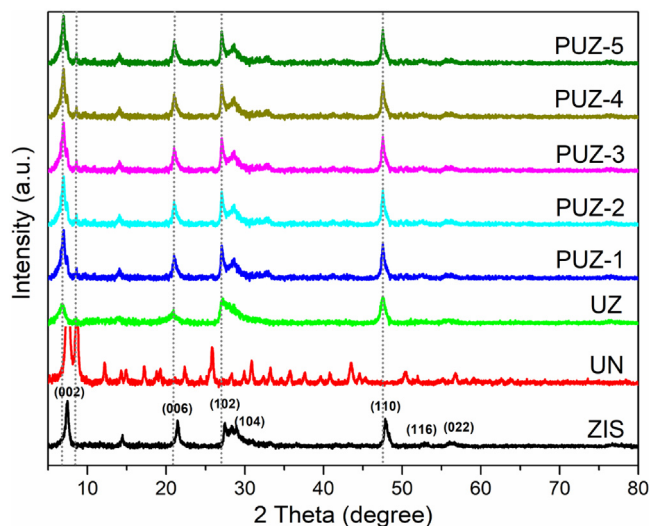

Fig. 1. XRD patterns of different photocatalysts.

PU-x and PUZ-x catalysts will be confirmed by TEM, XPS, and other methods in the following.

Figs. 2 and S2 show the morphology of different photocatalysts by SEM and TEM analyses. In Fig. 2(a), it can be observed that the as-synthesized pure UN are octahedron with an average size of about 100 nm. The UN is loaded with Pd NPs of about 5 nm as shown in Fig. 2(b). The morphology of PUZ-3 is a three-dimensional flower-like microsphere with a diameter of about 3−5 μm assembled by many nanosheets. And it is found that the PU nanoparticles distribute among the nanosheets uniformly. However, it is hard to find Pd NPs in the SEM images of PUZ due to the small size of Pd.

More details of the microstructure of catalysts are shown in Figs. 3 and S3. Fig. 3(a) and (b) shows the presence of UN, ZIS, and Pd in composites. Pd NPs are successfully loaded on UN octahedron, and some Pd NPs enter the interior of UN through the pores, indicating that Pd NPs are dispersed both inside and outside of UN (Fig. S3(b)). The HRTEM image (Fig. 3(c)) of PUZ-3 displays the clear lattice fringes with the distance of 0.32 nm, coinciding with the value for the (102) plane of ZIS [42], and it also shows the interplanar spacing of 0.23 nm corresponding to the (111) plane of *fcc* Pd [43], which confirms the existence of metallic Pd. Furthermore, by utilizing energy dispersive X-ray (EDX) elemental mapping (Fig. 3(d)), Zr, In, Zn, S, and Pd elements emerge in the PUZ-3 composites, offering convincing evidence of the successful combination of Pd NPs, UN and ZIS. Especially, Zn, In and S are distributed uniformly while N, Pd, and Zr are mainly concentrated in the interior of the composites (Fig. 3(g–l)). It can be seen obviously that Pd NPs agglomerate inside the composites, but there also shows the Pd signal in the outer layer of the whole flower-like microspheres. Based on the above results, it is suggested that Pd NPs, UN, and ZIS are well crystallized, and close contact among Pt NPs, UN, and ZIS is noticed, which contributes to the separation of photogenerated electrons and holes.

FT-IR spectra can further demonstrate the formation of PU and PUZ photocatalysts. As shown in Fig. 4(a), the FT-IR spectra of PU-x have similar characteristic peaks to UN, showing double peaks at about 3462 and 3338 cm^{-1}, corresponding to the asymmetric and symmetric stretching vibrations of -NH$_2$ functional groups, respectively [44]. In the lower wavenumber region, there are two peaks at about 1661 and 1257 cm^{-1}, which are respectively attributed to the N−H bending vibration of aromatic amines and the characteristic C−N stretching vibration [45]. However, in the FT-IR spectra of PU-x catalysts (Fig. 4(b) and (c)), it is found that the unsymmetrical tensile vibration and bending vibration of -NH$_2$ functional
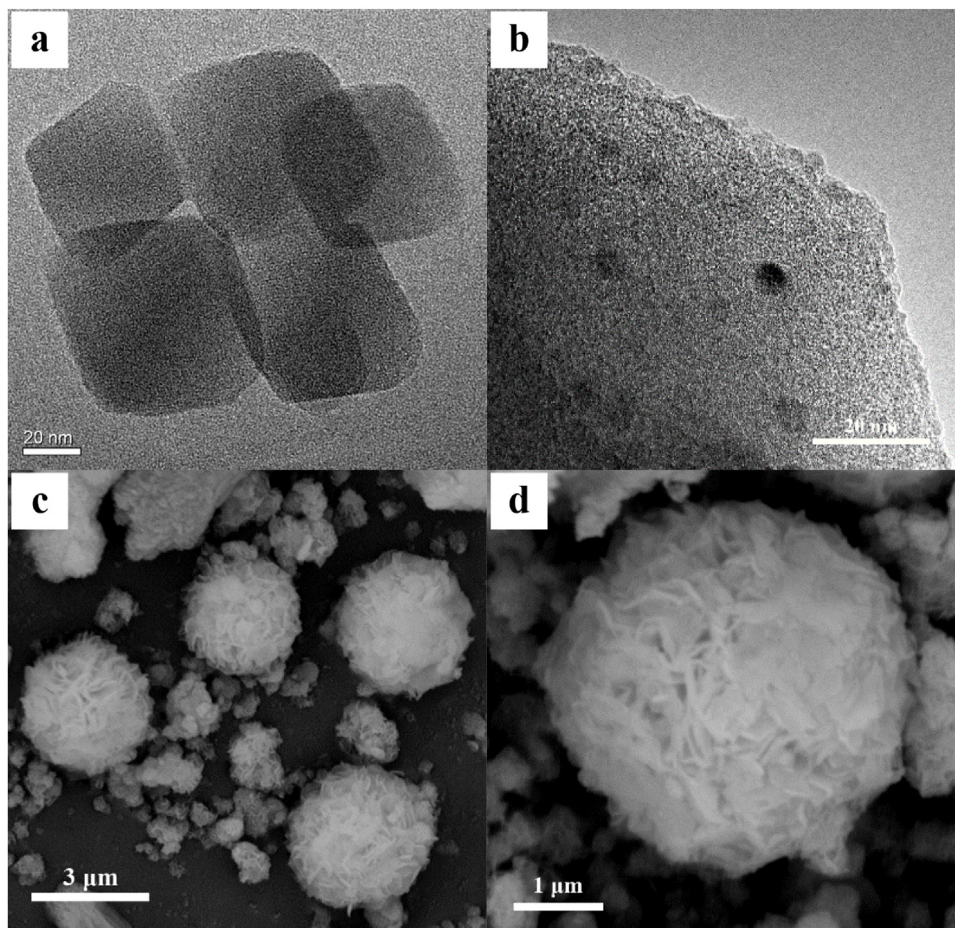
Fig. 2. (a) TEM image of UN, (b) TEM image of PU, (c, d) SEM images of PUZ.

groups at 3462 and 1661 cm^{-1} shift to a low wavenumber region compared with UN, which may be the effect of Pd NPs. Similarly, in the spectra of PUZ-*x* composites, there are characteristic peaks corresponding to benzene ring C=C vibration at about 1496 cm^{-1} (Fig. 4(e)) [46], which is difficult to be observed on UZ, indicating that UN in PUZ-*x* catalysts maintains complete MOFs structure after compositing with other semiconductors, and they have close contact as expected.

X-ray photoelectron spectroscopy (XPS) is a surface research technique, which can be used to determine the oxidation states of all elements in composite materials. Fig. 5(a) shows the survey spectra of UN, PU-3, ZIS and PUZ-3 samples, with no other impurity peaks observed. It should be emphasized that the Pd 3d signal in PU-3 and PUZ-3 confirms the successful loading of Pd element into UN and ZIS. The C 1s spectrum shows three peaks at 284.6, 286.7, and 288.9 eV (Fig. 5(b)), corresponding to C=C, C-NH$_2$, and C=O, respectively [42]. In UN catalysts, the peaks of Zr 3$d_{5/2}$ and Zr 3$d_{3/2}$ are located at 182.8 eV and 185.2 eV, while the peaks of Zr 3$d_{5/2}$ and Zr 3$d_{3/2}$ in PUZ-3 are located at 183.4 eV and 185.9 eV, respectively. The results prove that the binding energy shifts to a higher B.E. level and the electron density decreases of Zr element, implying a modulated local electronic structure of Zr cations in the presence of co-catalysts [47,48]. As shown in Fig. 5(d), peaks of Pd 3d in PU-3 is overlapped by Zr 3p, showing two peaks at 335.9 eV and 341.5 eV separately, belonging to the 3$d_{5/2}$ and 3$d_{3/2}$ orbits of Pd [49–51]. The two peaks at 333.3 eV and 346.9 eV belong to Zr 3$p_{3/2}$ and Zr 3$p_{1/2}$ orbits [39]. In PUZ-3 catalysts, due to the low content of Pd, it is hard to obtain accurate peaks of Pd. Fig. S4 shows the spectra of N 1s in PUZ-3, with two characteristic peaks of 399.4 eV and

402.4 eV, which are attributed to N atoms of the amino functionality stretching out or protruding into the cavities (-N=$^+$) and N with a positive charge (-NH-$^+$) on UN [42,52].

As for ZIS, there are two peaks centered at 445.6 eV (In 3$d_{5/2}$) and 453.2 eV (In 3$d_{3/2}$) assigned to In (+3) chemical state (Fig. 5(e)). The spectra of Zn 2p are deconvoluted into 1022.2 eV and 1045.2 eV in PUZ-3, ascribed to Zn 2$p_{3/2}$ and Zn 2$p_{1/2}$ (Fig. 5(f)). Furthermore, S 2p XPS spectra in Fig. 5(g) are deconvoluted into 162.5 eV and 163.8 eV, which match with S 2$p_{3/2}$ and S 2$p_{1/2}$ respectively. Compared to the pure ZIS, the peaks of In, Zn, and S XPS spectra in PUZ-3 migrate to higher binding energy, revealing that the electrons generated by the photo-excitation can be easily transmitted to the electron-rich Pd center [51], revealing the interaction among the Pd, UN, and ZIS. Pd doping can effectively improve the electron transfer efficiency, promote the separation of photogenerated electron hole pairs, and further improve the photocatalytic activity. These XPS results display the successfully loaded Pd element in the composites, and the effective interaction among Pd NPs, UN, and ZIS.

Brunauer-Emmett-Teller (BET) surface areas of UN, ZIS, UZ and PUZ-3 catalysts were analyzed by N$_2$ adsorption-desorption isotherms. In Fig. 6(a), it can be easily found that the isotherm of pure UN shows a type I pattern with a steep nitrogen gas uptake at low relative pressure, possessing microporous structure. Pure ZIS, UZ, and PUZ-3 have the isotherms of type IV pattern with H$_3$ type adsorption hysteresis loop without obvious saturated adsorption platform, proving the mesoporous structure of catalysts. The pore distribution of catalysts is displayed in Fig. 6(b). As we can see, the pore size of UN is approximately 2.49 nm, while the pore size of ZIS is about 12.2 nm, and the pore size of UZ is close to that
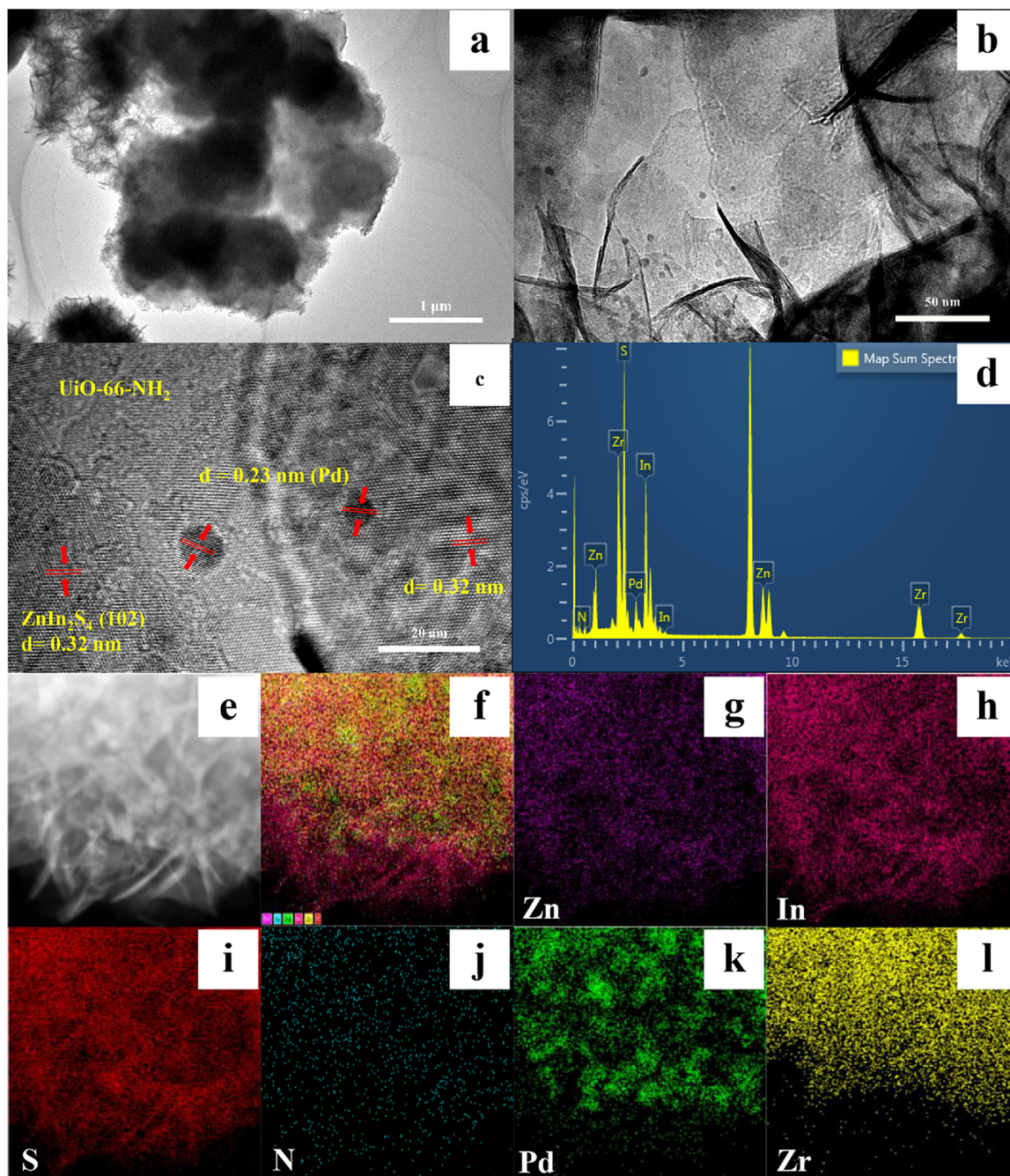
Fig. 3. (a, b) TEM, (c) HRTEM, (d) EDS pattern, and (e-l) mapping images of PUZ composites.

Table 1
The physical structural properties of UN, ZIS, UZ, and PUZ-3.

Sample	S_{BET} (m^2 g^{-1})	Pore volume (cm^3 g^{-1})	Average pore size (nm)
UN	732.5	0.46	2.49
ZIS	74.4	0.10	12.2
UZ	162.8	0.11	11.9
PUZ-3	165.2	0.32	7.79

of ZIS. The physical structural properties of UN, ZIS, UZ, and PUZ-3 catalysts are shown in Table 1. UN has the highest BET surface area of 732.5 m^2 g^{-1}, but it does not have the highest photocatalytic activity for the hydrogen production reaction, because it is related to not only the surface area but also the electron-hole pairs separation efficiency. The surface area of PUZ-3 increases with the

addition of PU-3, which is beneficial to exposing more active sites in composites and enhancing the photocatalytic activity.

Optical absorption properties have a crucial role in the photocatalytic activity of the catalysts, and we used Kubelka-Munk curve to get the band gap (E_g) of different samples as shown in Fig. 7. The absorption edge of UN at 450 nm and that of ZIS at 500 nm are around 2.88 and 2.54 eV, respectively, and the band gap of the UZ at 480 nm is about 2.61 eV. Compared with ZIS and UN, the absorption edge of UZ and PUZ-x samples is red-shifted obviously with the spectral response range expanding in the range of visible light, which shows that the interaction between UN and ZIS would form a heterojunction to broaden spectral response range [53]. Furthermore, Pd NPs with different ratios can also affect the intensity of light response, especially in the visible light region. The E_g of PUZ-1, PUZ-2, PUZ-3, PUZ-4, and PUZ-5 are 2.59, 2.53, 2.55, 2.54, and
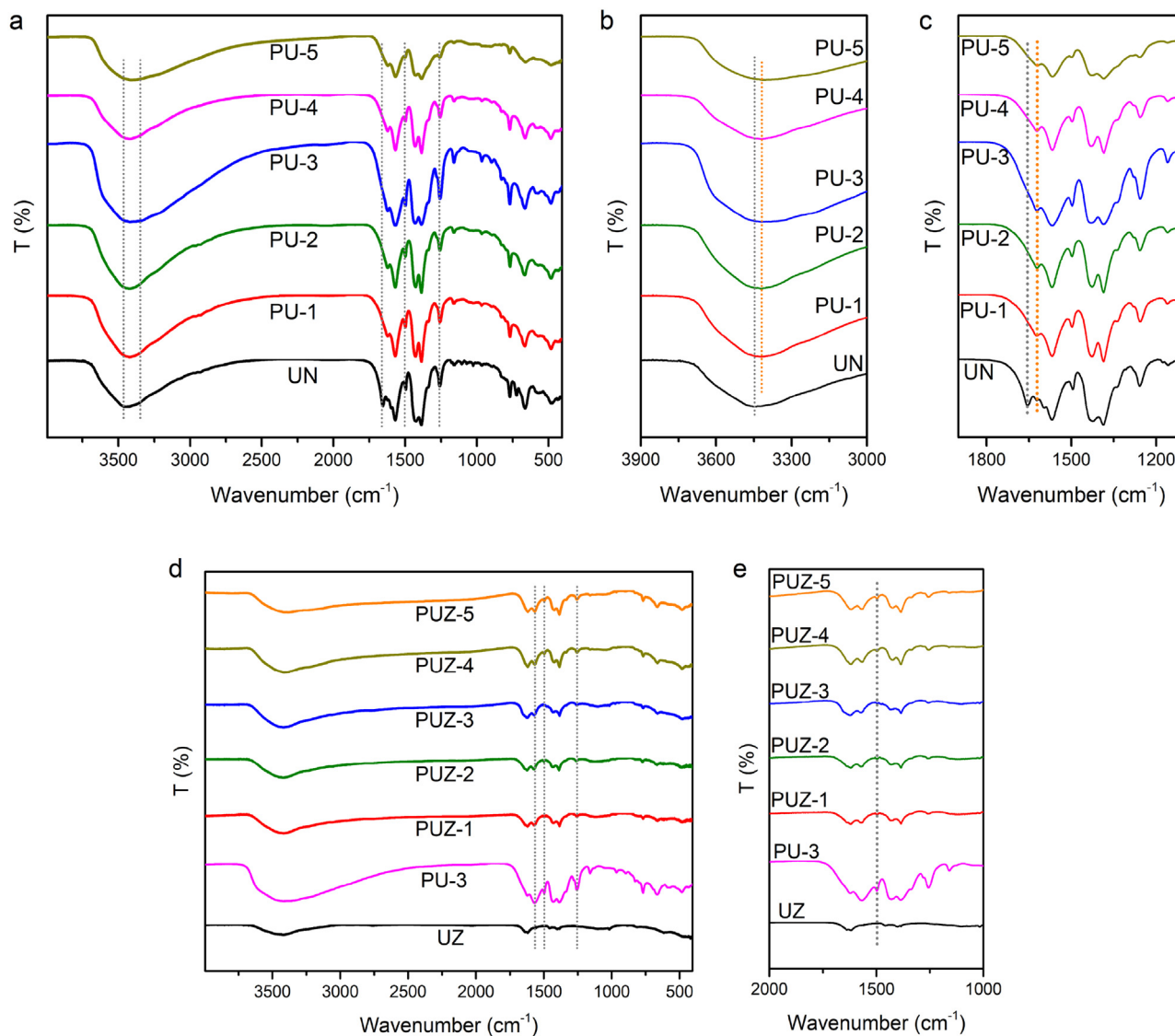
Fig. 4. FT-IR spectra of (a–c) PU-*x* and (d, e) PUZ-*x* catalysts.

2.61 eV, respectively. Obviously, with the addition of Pd NPs, the light absorption of the composite catalysts in the visible region is significantly enhanced, and the good contact among Pd NPs, UN, and ZIS results in a more pronounced shift in the Fermi level and a narrower band gap, which improves the utilization of visible light and further improves its photocatalytic activity.

3.2. Photocatalytic activity test

The photocatalytic properties of catalysts were studied by the photocatalytic hydrogen production reaction using TEOA as a sacrificial agent under visible light (λ > 420 nm). In Fig. S5(a) and (b), we tested a variety of noble metal-loaded catalysts, consisting of PtUZ, AgUZ, CuUZ, and PUZ under sunlight and visible light irradiation to confirm the hydrogen production activity. Obviously, the hydrogen production rate of PUZ samples is the highest, which proves that the Pd-loaded UN is an effective co-catalyst to promote the photocatalytic hydrogen production of ZIS, and the effect is better than Pt, Ag and Cu under the same experimental conditions.

Subsequently, the PUZ catalysts were further tested in the following experiments. As we can see in Fig. 8(a) and (b), PUZ-*x* samples have higher photocatalytic activity than UN, ZIS, and UZ,

which indicates that the doping of Pd NPs can greatly improve the photocatalytic hydrogen production. The hydrogen production of PUZ-*x* samples with different ratios shows a linear response in the irradiation time, showing the continuous and stable production of hydrogen. It is calculated that the photocatalytic hydrogen production rate of PUZ-*x* samples is significantly improved, especially when the Pd content is 0.3 %, reaching up to 5.26 mmol g^{-1} h^{-1}, which is about 17 and 3.8 times higher than that of pure ZIS and UZ, superior to most of the Zr-MOF-based photocatalysts (Table S1). Besides, too much Pd loading may lead to agglomeration of Pd NPs, and then affect the improvement of the catalytic activity. Compared with UZ, PUZ-*x* catalysts can effectively improve the utilization ratio and photocatalytic activity of solar energy, especially in the visible light region, and further improve the photocatalytic hydrogen production rate.

In addition, it is worth to note that the hydrogen production rate of PU-3 or Pd/ZIS is lower than that of PUZ-3 catalysts in Fig. 8(c), excluding the contributive part of Pd/UN or Pd/ZIS for the enhanced hydrogen production efficiency in PUZ composites. UZ with the same proportion of Pd or Pt (0.3 %) was also tested, and the activity has inferior performance than that of PUZ-3 catalysts. When PUZ-3 samples were added with 1% Pt nanoparticles as co-catalyst, the
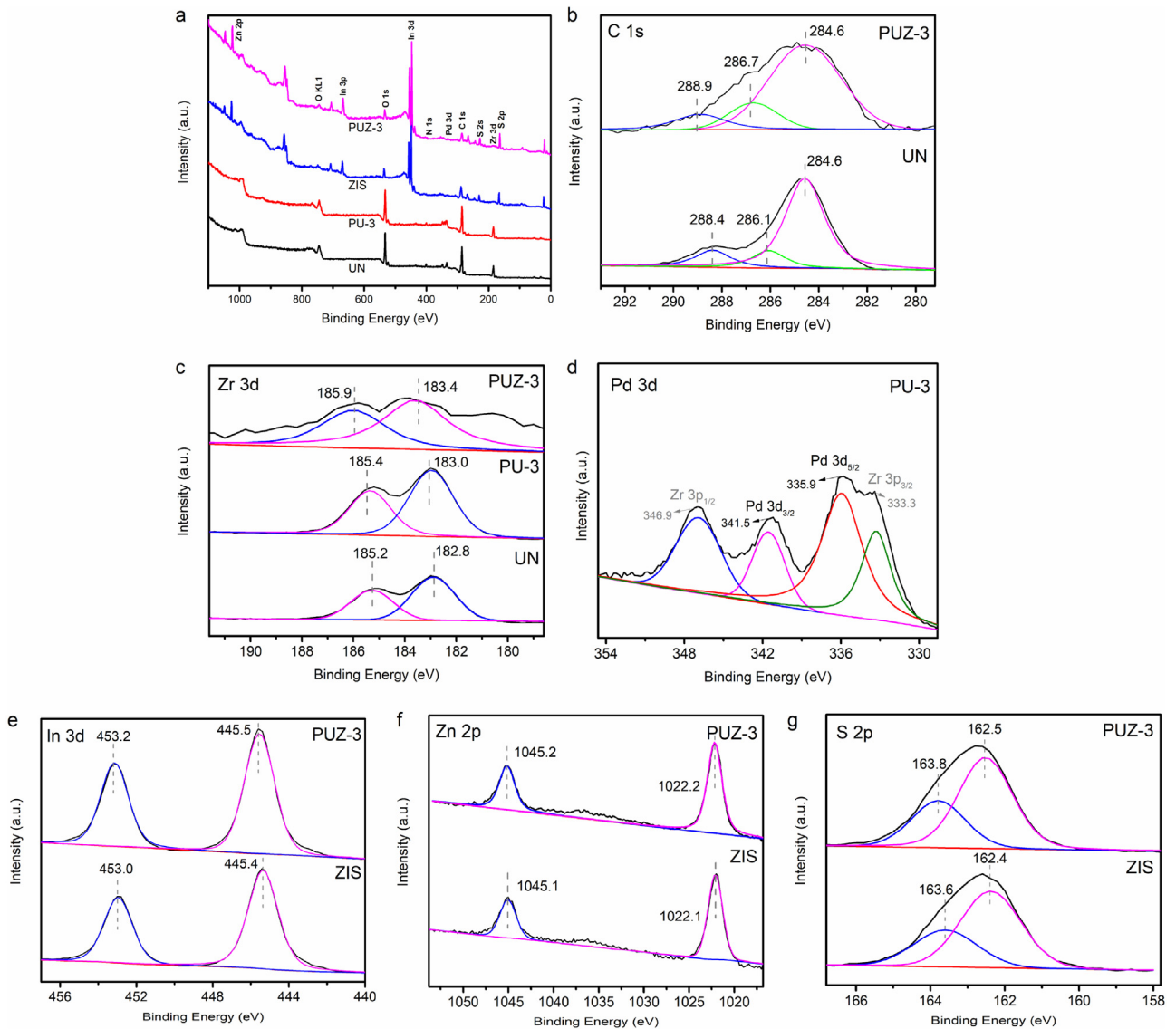
Fig. 5. XPS spectra of UN, PU-3, ZIS and PUZ-3: (a) survey spectra, (b) C 1*s*, (c) Zr 3*d*, (d) Pd 3*d*, (e) In 3*d*, (f) Zn 2*p*, and (g) S 2*p*.
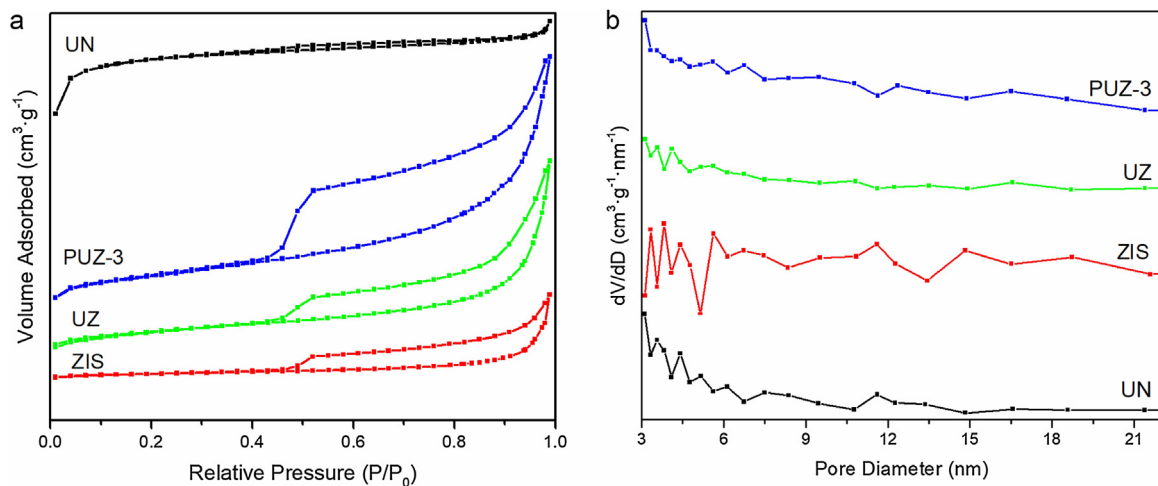

Fig. 6. (a) Nitrogen adsorption-desorption isotherms and (b) pore size distribution of UN, ZIS, UZ, and PUZ-3.
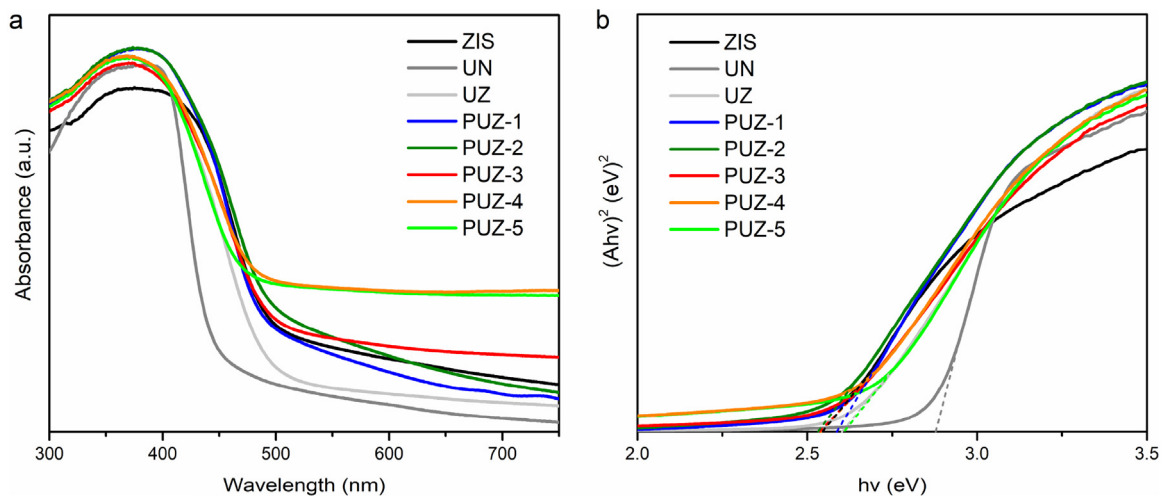
Fig. 7. (a) UV–vis. diffuse-reflectance spectra and (b) Kubelka-Munk curves of different photocatalysts.
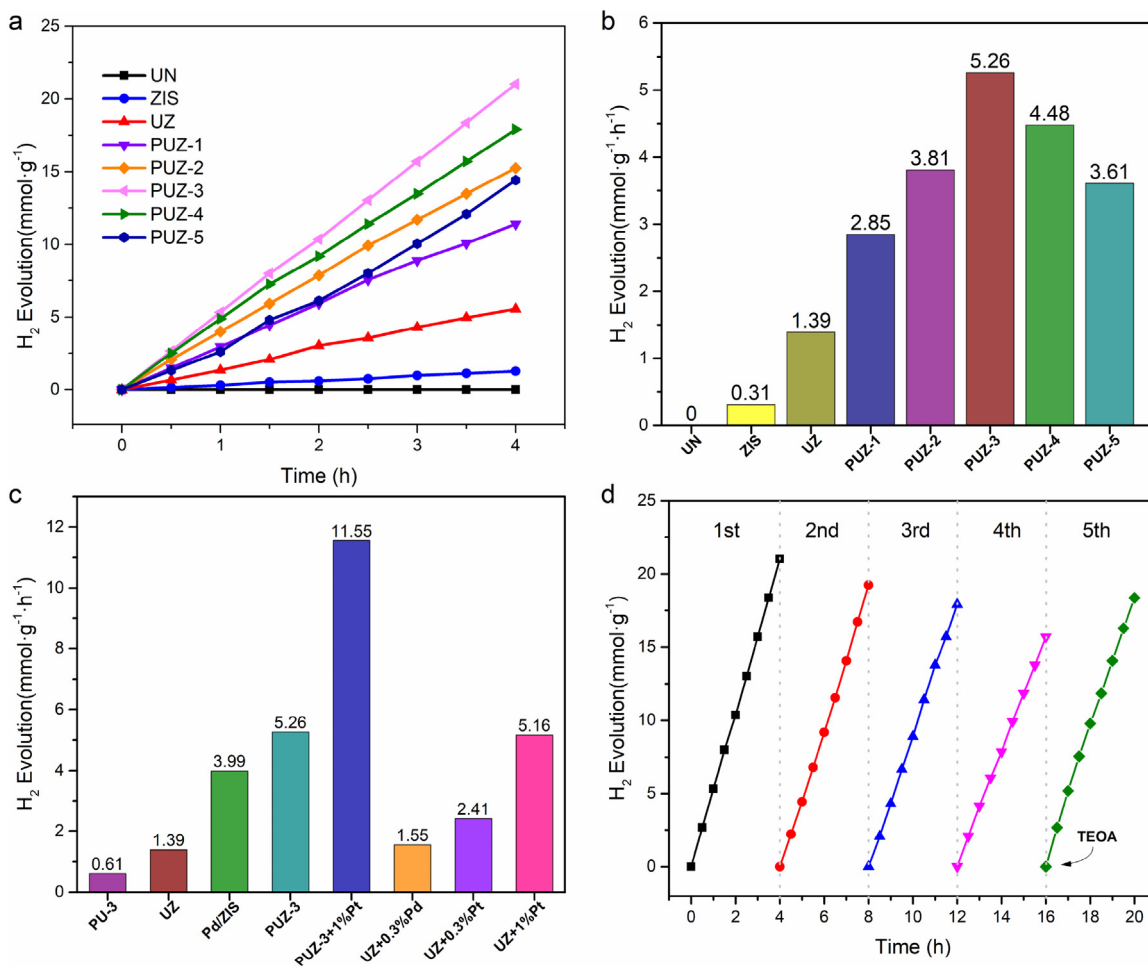

Fig. 8. (a) Photocatalytic hydrogen production under visible-light irradiation, (b, c) hydrogen production rates of various photocatalysts, and (d) reusability of PUZ-3 for the photocatalytic hydrogen production.

photocatalytic hydrogen production rate reached up to 11.55 mmol g^{-1} h^{-1} under visible light irradiation, which is 8.3 times higher than UZ, 2.3 times higher than UZ with 1 % Pt nanoparticles and 2.2 times higher than PUZ-3. Moreover, the photocatalytic hydrogen production rate of PUZ-3 and that of PUZ-3 with Pt nanoparticles as co-catalyst under simulated sunlight are 22.35 and 39.8 mmol

g^{-1} h^{-1} (Fig. S6). Under the existence of Pd and Pt, the synergistic effect may further fine-tune the hydrogen adsorption free energy of nanoparticles and promote electronic transmission [54,55], leading to an improved hydrogen evolution rate. At the same time, the QE is calculated as about 20.4 % at 320 nm and 3.2 % at 420 nm (Table 2). These results show that the as-designed PUZ-*x* catalysts

Table 2
The quantum efficiency (QE) for PUZ-3.

Wavelength (nm)	320	400	420	450
QE (%)	20.4	5.0	3.2	1.3

have the hierarchical structure of close contact interface and suitable band gap to promote the photocatalytic hydrogen production effectively.

The stability of the catalyst is another key factor in the practical application of high efficiency photocatalyst. Therefore, the photostability of PUZ-3 catalyst is further studied. As shown in Fig. 8(d), the optimized photocatalyst maintained excellent H_2 production stability during the cycling tests. The rate of H_2 production is 3.92 mmol g^{-1} h^{-1} after 4 cycles and 4.59 mmol g^{-1} h^{-1} after 5 cycles with 1 mL TEOA added, which is 87 % of the initial rate, still much higher than other catalysts in this system. In addition, comparing the XRD patterns, XPS spectra, and SEM images of the samples before and after five cycles of photocatalytic reaction, it is found that the crystal structure of PUZ-3 basically keeps its original state (Figs. S7 and S8).

3.3. Discussion

Photoluminescence (PL) spectra are usually used to study the excited states of semiconductor materials. It can provide information on charge carrier capture and recombination for PL emission [56]. Fig. 9(a) displays a comparison of the PL spectra of the catalysts. Under the excitation wavelength at 370 nm, there is a strong emission peak at 490 and 505 nm for pure ZIS. The luminescence spectra of UZ and PUZ-3 catalysts are similar to that of pure ZIS, but the fluorescence peak intensity decreases obviously. PL intensity decreases with the order of ZIS > UZ > PUZ-3, indicating that the composite rate of photocarriers is decreased. The peak intensity of PUZ-3 is the lowest, which proves that the photocarrier migration is the fastest, consistent with the results of photocatalytic hydrogen production. It reveals that PUZ-x catalysts are conducive to the separation and transfer of photocarriers, and then improve the photocatalytic activity.

In order to further study the separation and transfer efficiency of photocarriers, the photoelectric current intensity of ZIS, UZ, and PUZ-x samples was measured. Fig. 9(b) shows the photocurrent response results for five consecutive on-off cycles. It can be found that the photocurrent intensity of pure ZIS is the lowest, and UZ has a certain degree of enhancement. In the PUZ-x catalysts, the photocurrent intensities of PUZ-2, PUZ-3, and PUZ-4 are greater than that of UZ and ZIS, and PUZ-3 has the highest separation efficiency. Electrochemical impedance spectroscopy (EIS) is an effective method to characterize the transport characteristics of charge carriers. Fig. 9(c) shows the EIS-Nyquist curves of the catalysts, in which the arc radius of pure ZIS and UN is larger than that of UZ composites, and the radius of PU-3 is further reduced, while the arc radius of PUZ-3 is the smallest. The results show that the resistance of PUZ ternary composite catalysts is the lowest. For one thing, Pd doping is conducive to electron transfer and transport. For another, the composite of UN and ZIS enhances the effect of photocarrier separation, thus improving the activity of photocatalytic hydrogen production.

According to the Mott-Schottky curve, the flat band position of the semiconductor catalysts can be determined [57,58]. We analyzed the flat band potential of UN, ZIS, UZ, and PUZ-3 samples, and the positive slope of the obtained curve is consistent with that of a typical n-type semiconductor [59]. The flat band potentials of UN, ZIS, UZ, and PUZ-3 are shown in Figs. 10(a) and S9. For general n-type semiconductors, the conduction potential is 0.2 eV less than that of the flat band, while that of Ag/AgCl is 0.2 eV relative to the
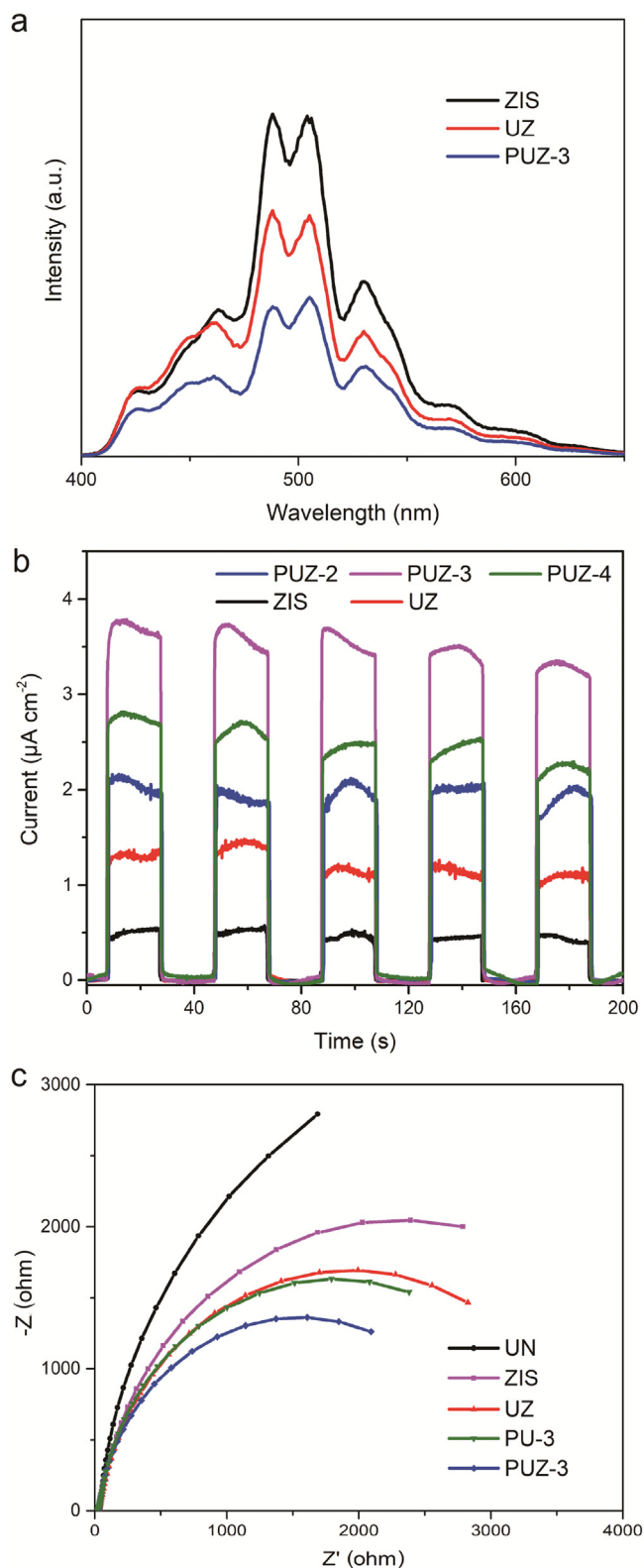
Fig. 9. (a) Photoluminescence emission spectra, (b) photocurrent, and (c) electrochemical impedance spectra of catalysts.

standard hydrogen potential [60,61], so the conduction potential of UN, ZIS, UZ and PUZ-3 samples is equivalent to −0.56, −0.92, −0.81 and −0.73 eV (vs. NHE), respectively. According to the calculation of UV–vis DRS, the band gaps of UN, ZIS, UZ, and PUZ-3 catalysts are 2.88, 2.54, 2.61, and 2.55 eV (vs. NHE), and the location of the
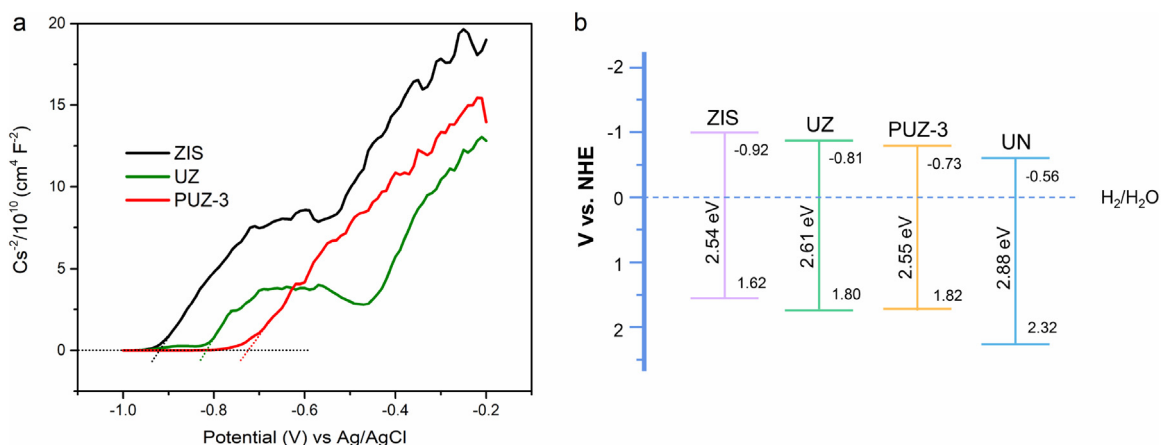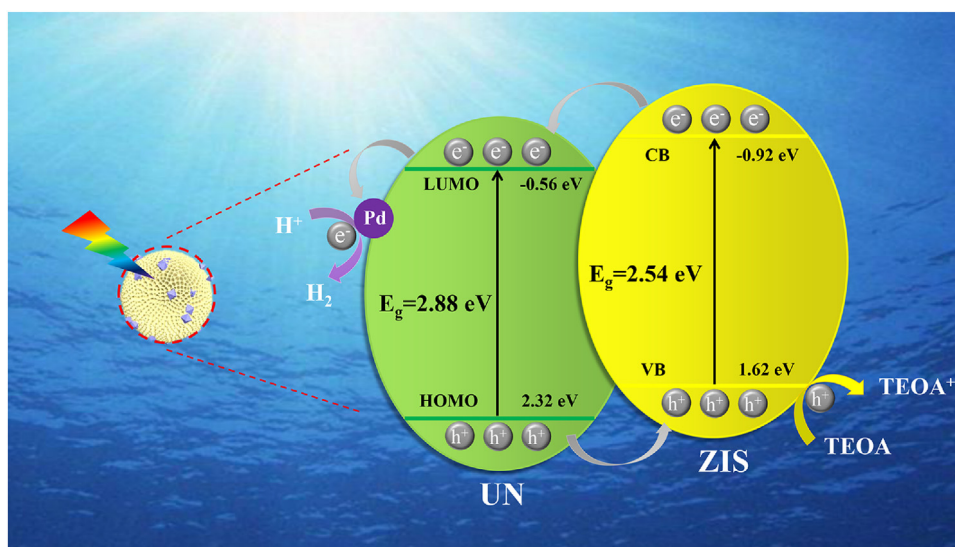
Fig. 10. (a) Electrochemical Mott-Schottky plots of ZIS, UZ and PUZ-3, (b) schematic illustration of band structures of UN, ZIS, UZ and PUZ-3.

Scheme 2. Schematic illustration of the mechanism of PUZ-3 during photocatalytic hydrogen evolution under sunlight irradiation.

valence band of UN, ZIS, UZ, and PUZ-3 are 2.32, 1.62, 1.80, and 1.82 eV (vs. NHE), respectively, which is consistent with VB spectra (Fig. S10). Based on the above discussions, the complete band structures of UN, ZIS, UZ, and PUZ-3 samples are shown in Fig. 10(b).

For the half-reaction of water reduction, the CB potential of catalysts must be more negative than the H_2/H_2O potential (0.0 V vs. NHE). In our work, Pd-loaded UN is an effective co-catalyst of ZIS to lower the activation energy barriers and promote the performance of photocatalytic hydrogen production. Based on the previous reports, the proposed mechanism of photocatalytic water reduction over PUZ-*x* composites under visible light irradiation is shown in Scheme 2.

In this study, high photocatalytic activity of hydrogen production is attributed to the reduced overpotential and formation of Schottky contact by Pd NPs on the surface of catalysts. Under the visible light illumination, the electrons on VB of ZIS are excited to CB, while electrons on the highest occupied molecular orbital (HOMO) of UN are excited to the lowest unoccupied molecular orbital (LUMO), creating holes on VB and HOMO. Photogenerated electrons on CB of ZIS can be transferred to LUMO of UN, for CB potential (−0.92 eV vs. NHE) of ZIS is more negative than LUMO potential (−0.56 eV vs. NHE) of UN. The localized surface plasmon resonance of the Pd NPs results in effective light absorption and generates more electrons. In addition, Pd has a work function of 5.1 eV, and UN has a work function of 4.1 eV. Thus, Schottky contact

could form at the interface between Pd and UN due to the difference in the work function, and drive electron migration from UN to Pd to produce H_2 at the active surfaces. A noble metal with a larger work function relative to the semiconductor can result in a stronger Schottky contact effect, and therefore a higher activity for hydrogen evolution [62,63]. In the above process, the introduction of Pd NPs can improve the absorption and response to light, making the catalyst produce more electrons and holes. At the same time, Pd NPs contribute to the transfer and transmission of photogenerated electrons in the system. Due to the existence of sacrificial agents, the rate of photocatalytic hydrogen production mainly depends on the number of photo generated electron-hole pairs and the rate of electron transport. Therefore, the interaction of Pd, UN, and ZIS in the ternary composites contributes to the significant improvement of the photocatalytic performance of the composite catalyst.

4. Conclusion

In this work, a novel facile method of successfully synthesizing Pd-loaded UiO-66-NH$_2$ octahedron encapsulated in flower-like microsphere ZnIn$_2$S$_4$ is reported. In the photocatalytic hydrogen production, 0.3 % Pd@UiO-66-NH$_2$@ZnIn$_2$S$_4$ composite exhibits 17-fold higher activity than pristine ZnIn$_2$S$_4$, reaching up to 5.26 and 22.35 mmol g^{-1} h^{-1} under visible light and simulated sunlight

irradiation. The quantum efficiency (QE) value of 0.3 % Pd@UiO-66-NH$_2$@ZnIn$_2$S$_4$ reaches 20.4 % and 3.2 % at the wavelength of 320 and 420 nm, respectively. The notably enhanced photocatalytic activity is ascribed to the unique structure of Pd@UiO-66-NH$_2$ @ZnIn$_2$S$_4$ composites. UiO-66-NH$_2$ and ZnIn$_2$S$_4$ have close contact interface and suitable band gap, which can effectively improve the utilization of visible light. Moreover, the introduction of Pd NPs can not only broaden the spectral response range of the composite catalyst but also promote the photon-induced charge carrier separation and prolong the lifetime of photon-induced charge carriers. The present work might provide a useful strategy for further development of efficient hydrogen photocatalysts.

Declaration of Competing Interest

There are no conflicts to declare.

Acknowledgements

Appendix A. Supplementary data

Supplementary material related to this article can be found, in the online version, at doi:https://doi.org/10.1016/j.jmst.2020.11.028.

References

[1] J.K. Stolarczyk, S. Bhattacharyya, L. Polavarapu, J. Feldmann, ACS Catal. 8 (2018) 3602–3635.
[2] F.E. Osterloh, Chem. Soc. Rev. 43 (2013) 2294–2320.
[3] Z. Wang, C. Li, K. Domen, Chem. Soc. Rev. 48 (2019) 2109–2125.
[4] X. Wang, K. Maeda, A. Thomas, K. Takanabe, G. Xin, J.M. Carlsson, K. Domen, M. Antonietti, Nat. Mater. 8 (2009) 76–80.
[5] L. Pan, J.H. Kim, M.T. Mayer, M.K. Son, A. Ummadisingu, J.S. Lee, A. Hagfeldt, J. Luo, M. Grätzel, Nat. Catal. 1 (2018) 412–420.
[6] J. Yu, A. Kudo, Adv. Funct. Mater. 16 (2016) 2163–2169.
[7] C.M. Wolff, P.D. Frischmann, M. Schulze, B.J. Bohn, R. Wein, P. Livadas, M.T. Carlson, F. Jäckel, J. Feldmann, F. Würthner, J.K. Stolarczyk, Nat. Energy 3 (2018) 862–869.
[8] J. Ren, W. Wang, S. Sun, L. Zhang, J. Chang, Appl. Catal. B 92 (2009) 50–55.
[9] Y. Liu, Y. Li, F. Peng, Y. Lin, S. Yang, S. Zhang, H. Wang, Y. Cao, H. Yu, Appl. Catal. B 241 (2018) 236–245.
[10] Z. Wang, Y. Inoue, T. Hisatomi, R. Ishikawa, Q. Wang, T. Takata, S. Chen, N. Shibata, Y. Ikuhara, K. Domen, Nat. Catal. 1 (2018) 756–763.
[11] W.J. Youngblood, S.H.A. Lee, K. Maeda, T.E. Mallouk, Acc. Chem. Res. 42 (2009) 1966–1973.
[12] J. Willkomm, K.L. Orchard, A. Reynal, E. Pastor, J.R. Durrant, E. Reisner, Chem. Soc. Rev. 45 (2016) 9–23.
[13] X. Wang, K. Maeda, A. Thomas, K. Takanabe, G. Xin, J.M. Carlsson, K. Domen, M. Antonietti, Nat. Mater. 8 (2009) 76–80.
[14] S. Shen, Qi. Wang, Chem. Mater. 25 (2013) 1166–1178.
[15] B. Mao, C.H. Chuang, J. Wang, C. Burda, J. Phys. Chem. C 115 (2011) 8945–8954.
[16] C.J. Xing, Y.J. Zhang, W. Yan, L.J. Guo, Int. J. Hydrogen Energy 31 (2006) 2018–2024.
[17] L. Shang, C. Zhou, T. Bian, H. Yu, L.Z. Wu, C.H. Tung, T. Zhang, J. Mater. Chem. A 1 (2013) 4552–4558.
[18] W. Yang, L. Zhang, J. Xie, X. Zhang, Q. Liu, T. Yao, S. Wei, Q. Zhang, Y. Xie, Angew. Chem. Int. Ed. 55 (2016) 6716–6720.
[19] L. Zeng, X. Guo, C. He, C. Duan, ACS Catal. 6 (2016) 7935–7947.
[20] B. Liu, X. Liu, J. Liu, C. Feng, Z. Li, C. Li, Y. Gong, L. Pan, S. Xu, C.Q. Sun, Appl. Catal. B 226 (2018) 234–241.
[21] H. Du, R.M. Kong, X. Guo, F. Qu, J. Li, Nanoscale 10 (2018) 21617–21624.
[22] H. Wang, X.Z. Yuan, Y. Wu, G.M. Zeng, X.H. Chen, L.J. Leng, Z.B. Wu, L.B. Jiang, H. Li, J. Hazard. Mater. 286 (2015) 187–194.
[23] X.B. Wang, J. Liu, S. Leong, X.C. Lin, J. Wei, B. Kong, Y.F. Xu, Z.X. Low, J.F. Yao, H.T. Wang, ACS Appl. Mater. Interfaces 8 (2016) 9080–9087.
[24] R. Li, J.H. Hu, M.S. Deng, H.L. Wang, X.J. Wang, Y.L. Hu, H.L. Jiang, J. Jiang, Q. Zhang, Y. Xie, Y.J. Xiong, Adv. Mater. 26 (2014) 4783–4788.
[25] Y.L. Xu, M.M. Lv, H.B. Yang, Q. Chen, X.T. Liu, F.Y. Wei, RSC Adv. 5 (2015) 43473–43479.
[26] Z. Sha, J. Sun, H. Chan, S. Jaenicke, J. Wu, RSC Adv. 4 (2014) 64977–64984.
[27] Z. Sha, J.S. Wu, RSC Adv. 5 (2015) 39592–39600.
[28] R. Wang, L.N. Gu, J.J. Zhou, X.L. Liu, F. Teng, C.H. Li, Y.H. Shen, Y.P. Yuan, Adv. Mater. Interfaces 2 (2015), 1500037.
[29] L.J. Shen, S.J. Liang, W.M. Wu, R.W. Liang, L. Wu, J. Mater. Chem. A 1 (2013) 11473–11482.
[30] L.J. Shen, M.B. Luo, Y.H. Liu, R.W. Liang, F.F. Jing, L. Wu, Appl. Catal. B 166 (2015) 445–453.
[31] Y. Su, Z. Zhang, H. Liu, Y. Wang, Appl. Catal. B 200 (2017) 448–457.
[32] J.D. Xiao, H.L. Jiang, Acc. Chem. Res. 52 (2019) 356–366.
[33] L. Jiao, H.L. Jiang, Chem 5 (2019) 786–804.
[34] K. Wu, J. Chen, J.R. McBride, T. Lian, Science 349 (2015) 632–635.
[35] S. Han, S.C. Warren, S.M. Yoon, C.D. Malliakas, X. Hou, Y. Wei, M.G. Kanatzidis, B.A. Grzybowski, J. Am. Chem. Soc. 137 (2015) 8169–8175.
[36] C.H. Hendon, D. Tiana, A. Walsh, Phys. Chem. Chem. Phys. 14 (2012) 13120–13132.
[37] M.E. Foster, J.D. Azoulay, B.M. Wong, M.D. Allendorf, Chem. Sci. 5 (2014) 2081–2090.
[38] Q. Liang, J. Jin, C. Liu, S. Xu, C. Yao, Z. Li, Inorg. Chem. Front. 5 (2018) 335–343.
[39] D. Sun, Z. Li, J. Phys. Chem. C 120 (2016) 19744–19750.
[40] L. Shen, W. Wu, R. Liang, R. Lin, L. Wu, Nanoscale 5 (2013) 9374–9382.
[41] C. Chen, D. Chen, S. Xie, H. Quan, X. Luo, L. Guo, ACS Appl. Mater. Interfaces 9 (2017) 41043–41054.
[42] H. Liu, J. Zhang, D. Ao, Appl. Catal. B 221 (2018) 433–442.
[43] M. Lou, R. Wang, J. Zhang, X. Tang, L. Wang, Y. Guo, D. Jia, H. Shi, L. Yang, X. Wang, Z. Sun, T. Wang, Y. Huang, ACS Appl. Mater. Interfaces 11 (2019) 6431–6441.
[44] S. Wan, Q. Zhong, M. Ou, S. Zhang, J. Mater. Sci. 52 (2017) 11453–11466.
[45] M. Kandiah, M.H. Nilsen, S. Usseglio, S. Jakobsen, U. Olsbye, M. Tilset, C. Larabi, E.A. Quadrelli, F. Bonino, K.P. Lillerud, Chem. Mater. 22 (2010) 6632–6640.
[46] B. Li, Z. Guan, W. Wang, X. Yang, J. Hu, B. Tan, T. Li, Adv. Mater. 24 (2012) 3390–3395.
[47] F. Yang, Q. Zhang, J. Zhang, L. Zhang, M. Cao, W.L. Dai, Appl. Catal. B 278 (2020), 119290.
[48] X. Li, G. Yang, S. Li, N. Xiao, N. Li, Y. Gao, D. Lv, L. Ge, Chem. Eng. J. 379 (2020) 122350.
[49] A.F. Lee, J.N. Naughton, Z. Liu, K. Wilson, ACS Catal. 2 (2012) 2235–2241.
[50] I. Cho, V.T. Chen, S. Qiao, W. Koo, R.M. Penner, I. Kim, ACS Sens. 3 (2018) 2152–2158.
[51] X. Pan, H. Xu, X. Zhao, H. Zhang, ACS Sustainable Chem. Eng. 8 (2020) 1087–1094.
[52] H. Wang, X.Z. Yuan, Y. Wu, G.M. Zeng, X.H. Chen, L.J. Leng, H. Li, Appl. Catal. B 174 (2015) 445–454.
[53] C. Zhao, Y. Zhang, H. Jiang, J. Chen, Y. Liu, Q. Liang, M. Zhou, Z. Li, Y. Zhou, J. Phys. Chem. C 123 (2019) 18037–18049.
[54] M. Luo, P. Lu, W. Yao, C. Huang, Q. Xu, Qi. Wu, Y. Kuwahara, H. Yamashita, ACS Appl. Mater. Interfaces 8 (2016) 20667–20674.
[55] R. Su, R. Tiruvalam, A.J. Logsdail, Q. He, C.A. Downing, M.T. Jensen, N. Dimitratos, L. Kesavan, P.P. Wells, R. Bechstein, H.H. Jensen, S. Wendt, C.R.A. Catlow, C.J. Kiely, G.J. Hutchings, F. Besenbacher, ACS Nano 8 (2014) 3490–3497.
[56] H.Q. Xu, S. Yang, X. Ma, J. Huang, H.L. Jiang, ACS Catal. 12 (2018) 11615–11621.
[57] K. Gelderman, L. Lee, S.W. Donne, J. Chem. Educ. 84 (2007) 685–688.
[58] B. Bera, A. Chakraborty, T. Kar, P. Leuaa, M. Neergat, J. Phys. Chem. C 121 (2017) 20850–20856.
[59] Y. Liao, B. Yuan, D. Zhang, J. Zhang, X. Wang, P. Deng, K. Zhang, H. Zhang, Q. Xiang, Z. Zhong, Inorg. Chem. 57 (2018) 10249–10256.
[60] Z. Zhang, J. Long, L. Yang, W. Chen, W. Dai, X. Fu, X. Wang, Chem. Sci. 2 (2011) 1826–1830.
[61] K. Maeda, K. Sekizawa, O. Ishitani, Chem. Commun. 49 (2013) 10127–10129.
[62] E. Hussain, I. Majeed, M.A. Nadeem, A. Badshah, Y. Chen, M.A. Nadeem, R. Jin, J. Phys. Chem. C 120 (2016) 17205–17213.
[63] C.H. Hao, X.N. Guo, M. Sankar, H. Yang, B. Ma, Y.F. Zhang, X.L. Tong, G.Q. Jin, X.Y. Guo, ACS Appl. Mater. Interfaces 10 (2018) 23029–23036.